

Electron emission from deep traps in HfO₂ under thermal and optical excitationRoman Izmailov^{1,2}, Jack Strand^{3,4}, Nicolo' Ronchi,¹ Alexander Shluger^{3,5} and Valeri Afanas'ev^{1,2}
¹*imec, Kapeldreef 75, 3001 Leuven, Belgium*²*Department of Physics and Astronomy, KU Leuven, 3001 Leuven, Belgium*³*Department of Physics and Astronomy, University College London, Gower Street, London WC1E 6BT, United Kingdom*⁴*Nanolayers Research Computing Ltd., London, United Kingdom*⁵*WPI-Advanced Institute for Materials Research (WPI-AIMR), Tohoku University, 2-1-1 Katahira, Aoba-ku, Sendai 980-8577, Japan* (Received 15 December 2023; revised 21 March 2024; accepted 25 March 2024; published 17 April 2024)

The ratio between the energies of optical and thermal ionization depends on the defect nature and the strength of the interaction of trapped electrons with phonons. Knowing this ratio for a certain type of defect allows one to predict, e.g., thermal emission energies from the optically measured values. We present the results of direct empirical extraction of the ratio between optical and thermal electron emission energies for HfO₂ bulk electron traps combined with theoretical analysis of the physical mechanism of electron transitions from the trapped state to the mobility edge. We show that, by applying different excitation mechanisms, we affect the same deep traps inside the HfO₂ band gap; i.e., these traps are both optically and thermally active and are likely to have similar nature. The extracted empirical optical/thermal ionization energy ratio of 2.2 ± 0.3 is in good agreement with the polaronic nature of the probed electron traps, as shown by the results of theoretical calculations. Our results provide experimental and theoretical methodologies for consistently linking thermal and optical ionization energies of electron traps and describing their distributions in the band gap of amorphous oxides, and can help improve modeling frameworks for reliability issues related to oxide traps.

DOI: [10.1103/PhysRevB.109.134109](https://doi.org/10.1103/PhysRevB.109.134109)**I. INTRODUCTION**

HfO₂-based dielectric films are widely used in conventional high- κ metal gate (HKMG) field-effect transistors (FETs) [1,2] and various memory elements, such as dynamic random-access memory (DRAM) capacitors [3] and functional layers in different emerging memory types [4]. The latter include, among others, ferroelectric (FE) memories, following the breakthrough discovery of FE properties in thin doped HfO₂ films by Börscke and co-authors [5]. After being adopted by the semiconductor industry at the 45-nm technology node (replacing conventional low- κ gate oxides to enable further equivalent oxide thickness scaling) [6], HfO₂ films have been deeply integrated into the complementary metal-oxide-semiconductor (CMOS) technology [7] and, nowadays, exhibit excellent compatibility with production flows. However, with the introduction of HfO₂-based high- κ insulators into the core parts of microelectronic devices, significant reliability issues caused by charge trapping in these materials emerge. These include, in particular, positive and negative bias temperature instability (PBTi and NBTi, respectively) [8–12] in HKMG FETs as well as memory performance degradation in HfO₂-based FE FETs [13–16]. The urgent need to solve these problems led to extensive experimental

and theoretical studies of defects in these systems, especially those responsible for electron trapping in HfO₂-based systems, charging-discharging of which is primarily associated with the root cause for HKMG FET BTI [17] and ferroelectric degradation [13,14].

Among conventional defect spectroscopy methods, the most commonly used are electron-spin resonance (ESR) and charge injection and sensing (CIS) techniques, and their variations. CIS usually relies on drain current readouts and threshold voltage shift monitoring as a result of the carrier exchange between the semiconducting channel and near-interface traps under gate voltage stress and subsequent relaxation (i.e., zero gate voltage) conditions applied to the FET gate stack. The outcome of these measurements depends on the energy alignment of the trap levels with the Fermi level of semiconductor (usually, Si), effectively limiting the energy and spatial sensing range of this method to the portion of the semiconductor band gap and a narrow near-interface region of the gate dielectric, respectively [18]. ESR proved to be an extremely precise and efficient tool for studying various paramagnetic defects (for example, Si dangling bonds at Si/SiO₂ interface, so-called P_b centers [19]). However, hole trapping centers have been shown to be the only ESR-active centers in hafnia [20,21]. By combining CIS and ESR techniques, it is in principle possible to study stress-generated electron traps via electrically detected magnetic resonance (EDMR) [22], but so far no evidence of ESR-active electron trapping sites in the pristine HfO₂ layers has been reported in the literature.

On the other hand, the thermally and optically stimulated electron emission experiments [23–29] can access shallow

Published by the American Physical Society under the terms of the [Creative Commons Attribution 4.0 International](https://creativecommons.org/licenses/by/4.0/) license. Further distribution of this work must maintain attribution to the author(s) and the published article's title, journal citation, and DOI.

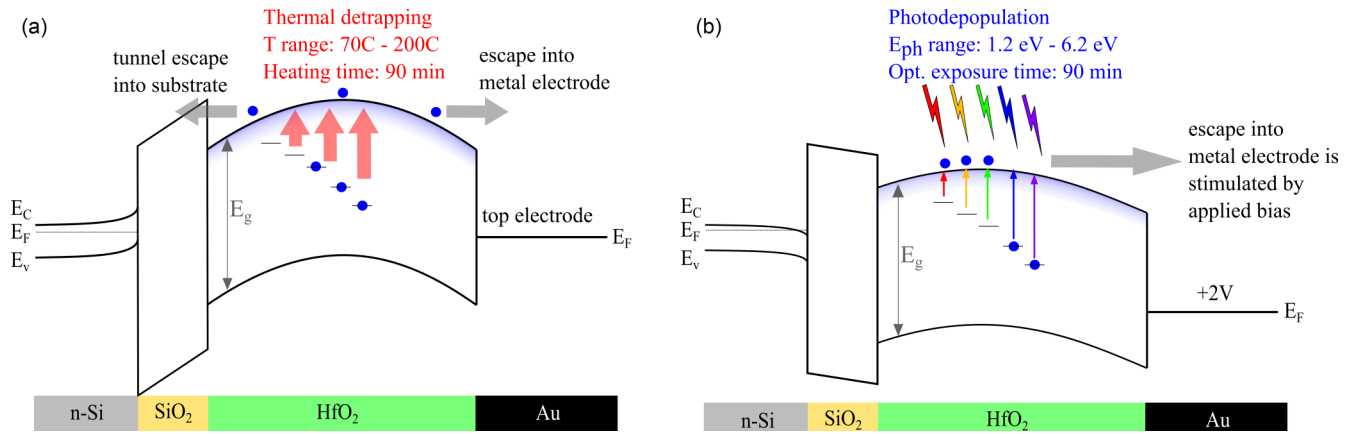


FIG. 1. Schematics of electron transitions during (a) thermal detrapping, and (b) optical EPDS experiments performed on n -Si/SiO₂/HfO₂/Au structures. Blue circles represent electrons; the ribbon near the HfO₂ CB indicates the existence of partially localized electronic states and the position of ME. The vertical colored arrows show the corresponding electron emission processes, while the gray horizontal arrows illustrate possible escape paths for electrons excited into HfO₂ CB or ME.

and deep traps in the wide energy range that covers the entire band gap of a high- κ insulator. To determine the trap energy distribution, this technique uses thermal- and photo-ionization (or photodepopulation) of filled electron traps into the conduction band (CB) where the excited electrons are pushed to a metal electrode by applying a bias. Therefore, one can describe this process as an electron *emission*. In HfO₂ films, measurements of thermally stimulated emission have been successfully used to reveal the presence of shallow traps located within 1.0 eV below the bottom of the HfO₂ CB (BCB) [26,27], while the optically stimulated emission probes deep trap levels with energy depth in the range of 1.5–5.6 eV with respect to the BCB [23–26,28,30].

However, direct comparison of the emission energies extracted from the shallow and deep traps poses a challenge as mechanisms of thermal and optical excitation of the same defect are different and the corresponding energies are not equal [26,29,31]. The ratio between the energies of the optical and thermal ionization processes, R , depends on the atomic structure of the defect and the strength of the interaction of trapped electrons with phonons. Knowing the value of R for a certain type of defect would allow, for example, one to estimate the thermal emission energies from the optically measured values. For small polarons in crystals, $R = 2.0$ is theoretically predicted [32,33] if polaron trapping is spontaneous and the effective mode frequency of the polaron (to be discussed later) does not change upon electron trapping. The R values calculated for hole polarons using density functional theory (DFT) are close to 2.0 [34–37] but differ significantly for point defects in solids where the optical and thermal ionization energies are much closer and R is often in the range of 1.2–1.5 for oxygen vacancies in oxides [38–44]. Therefore, R is indicative of the type of defects involved in electron trapping.

To shed more light on the nature and properties of electron traps in amorphous HfO₂ films, we measured their thermal and optical ionization (or detrapping) energies, as schematically illustrated in Figs. 1(a) and 1(b). The ribbon at the oxide BCB indicates the existence of partially localized electronic states in amorphous oxide and the position of the mobility

edge (ME) [45]. Electrons excited thermally (a) or optically (b) into the states close to the ME are swept by applying bias to a metal electrode. The temperature range of the thermal emission experiments [26,27] was expanded to probe the same deep traps that are available for exhaustive photodepopulation spectroscopy (EPDS) at room temperature [23,25,26,28]. This allowed us to directly determine the ratio R between the optical and thermal electron emission energies of the electron traps in α -HfO₂. The theoretical analysis of the physical mechanism of electron transitions from trapped states to ME is consistent with the polaronic character of the dominant electron traps in HfO₂.

The presented experimental methodology and theoretical explanation can be useful for improving the modeling framework aimed at trap-related reliability assessment of MOS devices with high- κ insulators. The extracted trap energy distribution in the wide energy range can serve as direct empirical reference which is important for validation of the existing models.

The outline of this paper is as follows. In the next section, we provide details of the experimental and theoretical methods used in this work. The experimental results for the thermal and optical excitation spectra of the traps in the α -HfO₂ films are presented in Sec. III. In Sec. IV we present a theoretical analysis and the results of calculations of thermal and optical emission energies for electron traps in α -HfO₂. Discussion of the results and conclusions are given in Sec. V.

II. MATERIALS AND METHODS

A. Experiment

Samples were fabricated by atomic layer deposition (ALD) of 20-nm-thick HfO₂ layers from HfCl₄ and H₂O precursors for Hf and O, respectively, at 300 °C on top of low-doped n -type (100) Si substrate with 5 nm of thermally grown SiO₂. Semitransparent (15-nm-thick) gold top electrodes of 0.5 mm² area were thermally evaporated through the mask ensuring no additional heating of the underlying structure. Similarly, a 1- μ m-thick Al layer was thermally evaporated on

the back side of the sample to provide electrical contact to the Si substrate.

These samples are known to have only a marginal density of occupied electron traps in the pristine state [25,28]. Therefore, to permit the characterization using trap emission spectroscopy, the traps first had to be filled with electrons. For this purpose, each sample was subjected to electron injection followed by long relaxation in the dark. Each of the steps is followed by 100 kHz capacitance-voltage (CV) curve recording to monitor the change in flat-band voltage (V_{FB}) which reflects the variation of charge trapped in the gate stack. This high-frequency limit of CV measurements was chosen to mitigate the impact of interface traps on V_{FB} and allows us to avoid significant errors due to series resistance [46]. Electron injection is performed by applying a sufficiently long (~ 500 ms) positive voltage pulse (+14 V) to the top Au electrode to ensure maximal filling of traps similarly as used in the previous study [26]. During the long postinjection relaxation in the dark under zero bias conditions, the trapped charge that is thermally unstable at room temperature is effectively removed from the film. As will be shown in the next section, relaxation for 48 hours already ensures good saturation of thermal detrapping kinetics. In emission experiments, the relaxation time was extended (up to ~ 2 weeks) to further reduce the V_{FB} drift.

We note that injection pulses of negative polarity applied to the metal gate may result in electron injection from the metal gate and hole injection from the silicon substrate, if sufficient substrate carrier density is provided (either by using a p -type substrate or illuminating the sample to photogenerate holes). However, the gate-side electron injection will be less pronounced than electron injection from the Si substrate side due to lack of electric field drop over high- κ oxide compared to low- κ SiO₂, and the hole injection from the substrate is hindered by substantially higher potential barrier at the Si-SiO₂ interface for hole tunneling (~ 4.5 eV) compared to electron tunneling (~ 3.1 eV) [47]. Moreover, the above mentioned injection processes due to negative gate voltage pulses are interfering with each other and, hence, less relevant to the trap spectroscopy experiments. Therefore, in the current study the injection experiments were limited to positive gate voltage pulses.

To enable accurate determination of R , the thermal detrapping experiments were repeated on a set of fully charged and relaxed capacitors at each elevated temperature. As illustrated in Fig. 1, panel (a), samples containing significant density of trapped electron charge were heated to different temperatures (ranging from 70 °C to 200 °C) for sufficiently long time (1.5 hours) to ensure the transition to the mobility edge of most trapped electrons accessible for thermal depopulation. Although most traps energetically available for thermal depopulation could be efficiently emptied at elevated temperature, it should be noted that not all of the thermally emitted electrons necessarily escape the high- κ film. Because in the heating setup the samples are disconnected from the measurement circuit, the top metal contact can be considered as a “floating” electrode. In this case, electrons that escape to the top electrode create a blocking field that may prevent other electrons from escaping the HfO₂ layer. At the end of the heating sequence, such electrons can be retrapped in bulk HfO₂

traps or, more likely, can populate traps near the SiO₂/HfO₂ interface, where a thin Hf _{x} Si_{1- x} O₂ layer may be present [48]. Nevertheless, a considerable fraction of charge escapes the film during heating, as indicated by a shift in a CV curve recorded before and after the heating step. To demonstrate the effect of the “floating” electrode condition, several samples were also subjected to heating while connected to the CV measurement setup, with or without positive bias applied to the top electrode.

To determine the optical energy value corresponding to the thermal emission energy at the given temperature, the heated samples were analyzed by EPDS at room temperature and compared with the EPDS spectra obtained on the unheated “reference” samples. The EPDS experiment, which is illustrated in Fig. 1(b) and is described in detail in Refs. [23–26,28], allows us to assess trap levels within narrow (~ 0.25 eV) optical energy intervals. In addition, we can avoid extra sample-to-sample variations in V_{FB} as compared to the case when different samples are used in thermal and optical excitation experiments. In the present work, during EPDS experiments, illumination time is set to 1.5 hours for each photon energy, ensuring saturation of the optical depopulation kinetics, while the top metal electrode was held either at 0 V or biased at +2 V to collect detrapped electrons.

B. Simulations

The density functional theory (DFT) calculations were carried out using the CP2K Quickstep code [49], which employs a primary linear combination of atomic orbitals (LCAO) basis set with an auxiliary plane-wave basis set. The Goedecker-Teter-Hutter (GTH) pseudopotentials and basis sets are used [50,51]. A double- ζ basis set is used for the valence electrons in all cases, with higher l orbitals used for polarization basis functions. An auxiliary plane-wave basis set with cutoff of 7875 eV is used. The hybrid density functional PBE0-TC-LRC [52] used to calculate the exchange-correlation (XC) energy has 0.25 Hartree-Fock exchange and an exchange cut-off radius of 4.0 Å [53]. The auxiliary density matrix method (ADMM) [54] improves the efficiency of calculations. All calculations are performed at the Γ point using a periodic cell of 324 atoms.

Amorphous structures were created using a technique described in detail in Refs. [53,55]. Using the melt-and-quench method, 360-atom periodic cells of crystalline HfO₂ were melted at 5000 K and then rapidly cooled, whereupon the system solidifies in a disordered arrangement. During the melt-and-quench process, interactions between atoms are described with the interatomic potentials developed in [56]. The disordered models were relaxed (both cell parameters and atomic coordinates) using the hybrid XC functional described above.

All defect structures are relaxed until forces are all below 2.4×10^{-3} eV Å⁻¹. In the calculation of the defect charge transition levels, we used the charge correction method of Ref. [57], which is based on the Lany-Zunger method [58]. The optical transition energies were calculated by taking the Franck-Condon energy difference between the potential energy curves (PEC) as described in detail in Sec. IV and using

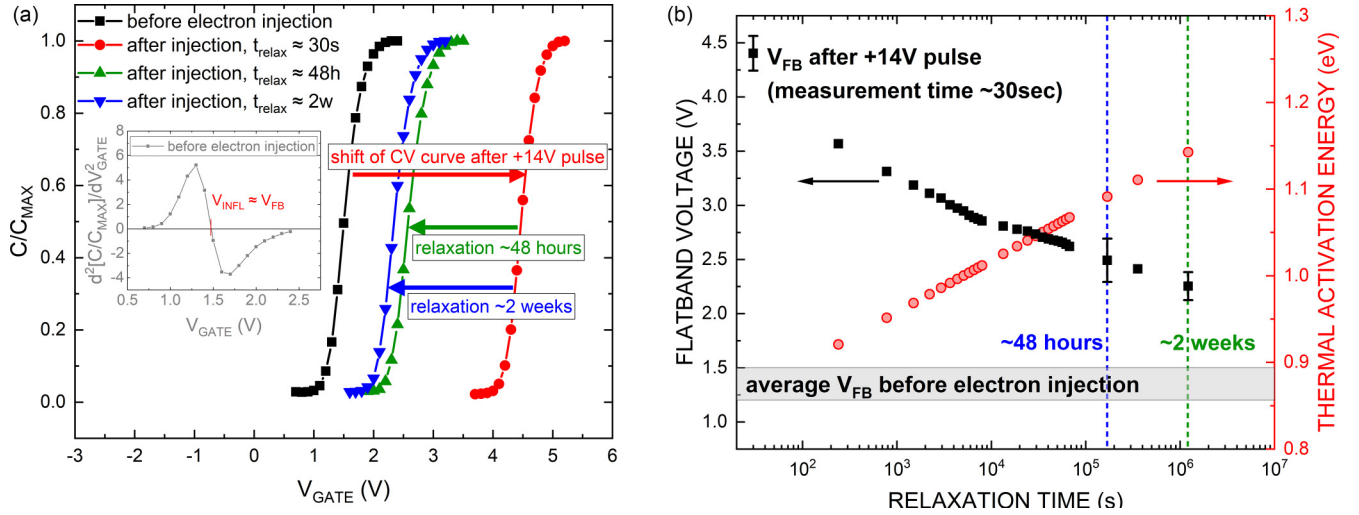


FIG. 2. (a) CV curves before/after electron injection and variable relaxation time. The inset illustrates how V_{FB} is extracted via the voltage inflection point method on the example of the initial state before electron injection. (b) Linear-log plot of V_{FB} relaxation in the dark at zero bias from the as-charged state (black squares, left axis). The error bars indicate the standard deviation across ~ 60 samples. Dashed lines indicate relaxation time of 48 hours (blue) and ~ 2 weeks (green). The red circles show the estimated thermal activation energy of trapped electrons on the corresponding timescale (right axis).

the time-dependent DFT (TDDFT) method implemented in CP2K [42].

III. EXPERIMENTAL RESULTS

A. Electron injection and trapped charge relaxation

As described in the previous section, before carrying out the electron emission experiments, samples were subjected to electron injection and subsequent relaxation in the dark under zero bias conditions. The example of CV curve evolution after charging and relaxation is illustrated in Fig. 2(a). After application of initial charging gate voltage pulse (+14 V) we observe significant increase of V_{FB} due to net electron trapping in the gate stack. It should be noted that the slow initial CV measurement already includes 30 s of relaxation time (i.e., some electrons manage to escape during the first CV measurement after injection). The negative shift of the CV curves during further relaxation indicates a continuous slow detrapping of electrons from the filled shallow traps. In this work we determine the numerical value of V_{FB} as the inflection point of the capacitance-voltage characteristic, V_{INFL} , which is a valid approximation (within 0.1 V accuracy) for the constant substrate doping and gate dielectric thickness [59]. The V_{FB} relaxation kinetics after +14 V charging pulse is shown in Fig. 2(b). It can be seen that extending the relaxation time to 2 weeks provides an extra V_{FB} shift of ~ 0.25 V, meaning that after 48 hours' relaxation at room temperature samples already reach 80%–90% saturation in thermal detrapping.

The nearly exponential decay of V_{FB} suggests that, at a given time, the main contribution to detrapping comes from a single trap level. Its thermal ionization energy can be estimated as $E_{th} = kT \ln(\nu\tau)$, where $kT \approx 26$ meV at $T = 300$ K, τ is the measurement time, and ν is the frequency factor, estimated as 10^{13} Hz for HfO₂ [26]. The calculated values for E_{th} shown on the right-hand axis of Fig. 2(b) demonstrate that, at the 48-hour mark, ≈ 2 the main trap level contributing

to the detrapping into the conduction band has the thermal ionization energy ≈ 1.1 eV. This corresponds to ≈ 2.2 – 2.4 eV optical emission energy as predicted in previous theoretical considerations [26,29,31].

B. Optical versus thermal depopulation

The validity of this estimate can be checked by comparing the EPDS spectra for identically processed and charged samples after relaxation for different times. The results are illustrated in Fig. 3 for three *n*-Si/5-nm SiO₂/20-nm HfO₂/15-nm Au samples subjected to +14 V electron injection pulse and variable relaxation time. The V_{FB} values, extracted from the CV curves similarly to 2(a), are plotted versus photon energy in panel (a) of Fig. 3. Corresponding values of spectral charge density (SCD, in $\text{cm}^{-2} \text{eV}^{-1}$) are directly extracted from the V_{FB} shift after each illumination step [23–26,28] and shown in Fig. 3(b), reflecting the trapped charge spectra sensed by the EPDS technique. As can be seen from this plot, the main energy level affected by extended relaxation at room temperature corresponds to ≈ 2.25 eV photon energy, which is in good agreement with the previous arguments.

As the next step, deep traps in the charged and relaxed samples were thermally probed by applying constant heating at 100 °C and 200 °C and monitoring the changes in the trapped charge density using the V_{FB} shift. These values, averaged over a set of samples, were then compared to the reference trapped charge density evolution observed in the EPDS experiments, as illustrated in Fig. 4. The EPDS spectra measured at 0 V bias during illumination can serve as a reliable reference for heating experiments, as these data are usually very reproducible (within 5%–10% accuracy) in the 1.5–3.1 eV photon energy range. On the other hand, the significant spread of the data in the heating-induced shift V_{FB} , caused by variations in the initial and relaxed V_{FB} positions, as suggested by the

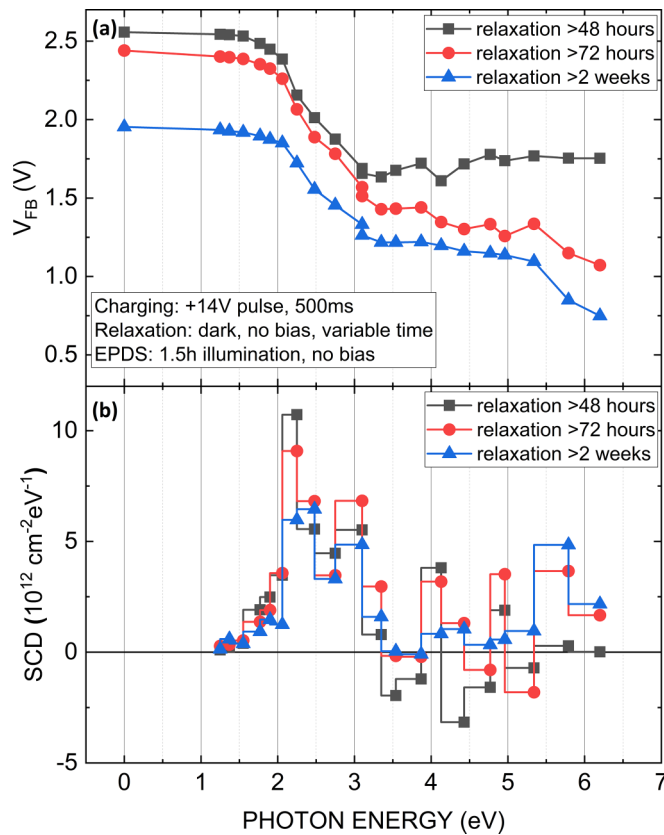


FIG. 3. Impact of variable relaxation time on the results of EPDS experiments as measured on identically processed *n*-Si/5-nm SiO₂/20-nm HfO₂/15-nm Au samples subjected to charge injection at +14 V. Panel (a) shows V_{FB} variation on the charged samples versus photon energy of incident illumination; panel (b) plots the corresponding SCD values for each energy interval. The detrapping peak at 2.25 eV photon energy is affected the most by the relaxation time variation, suggesting that the time constant of the thermal emission of electrons from this energy level at room temperature is comparable to the relaxation times used in the experiment.

relaxation kinetic data in Fig. 2(b), hinders the more accurate extraction of R . This outcome is somewhat expected in such experiments, as the defect density and the distribution profile change can be caused by the lateral nonuniformity of the pristine and charged samples, the presence of mobile ions (e.g., protonic species), and other factors. Furthermore, heating at 200 °C is likely at the limit of EPDS sensitivity. However, from the mean value of heating-induced charge loss, we can estimate the optical energy corresponding to the thermal transitions for each temperature using the simple expression $E_{th} \approx kT \ln(\nu\tau)$ (as in [26]), where τ is now equal to 90 minutes. For 100 °C we estimate $E_{th} \approx 1.25$ eV, and for 200 °C this yields $E_{th} \approx 1.57$ eV. Taking the interception points from Fig. 4, this corresponds to 2.5 eV and 3.1 eV, respectively, which gives the R value close to 2.

For the heating-EPDS sequence, the reference EPDS spectra measured on unheated samples can be used as a baseline. The corresponding spectral charge density of several samples versus photon energy (corresponding to the trapped electron energy below the mobility edge in HfO₂) is plotted in Fig. 5. It shows the change in the trapped charge density induced by

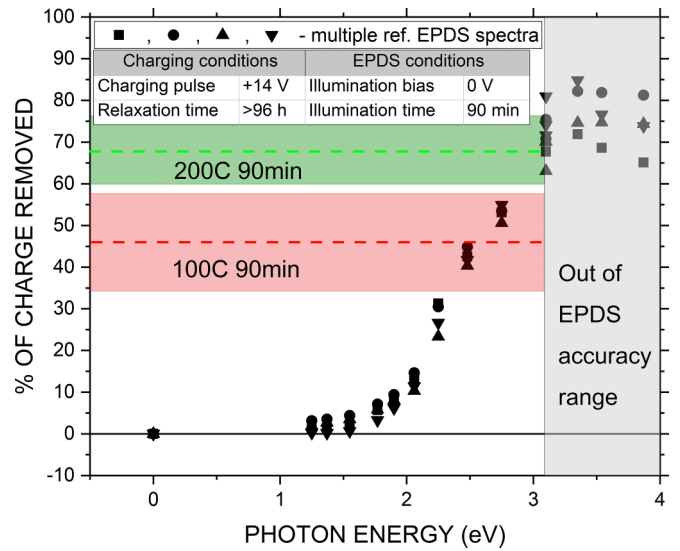


FIG. 4. Charge loss (in %) due to photodepopulation at zero bias versus the photon energy (black symbols) as measured on 4 equally processed *n*-Si/5-nm SiO₂/20-nm HfO₂/15-nm Au samples subjected to charge injection at +14 V and long relaxation in the dark. The gray area marks the photon energy range (above ≈ 3.1 eV) where EPDS accuracy decreases significantly. Red and green dashed lines illustrate the average percentage of trapped charge lost after heating at 100 °C and 200 °C, respectively, for 90 min, and the corresponding colored area illustrates the estimation error for the set of several samples.

photons with energies within a narrow interval, normalized by the width of this interval. These results are in good agreement with previously published data from the similarly prepared ALD HfO₂ samples [23,25,28]. The two well-known trap energy bands (at ≈ 2.25 eV below BCB and ≈ 3.1 eV below

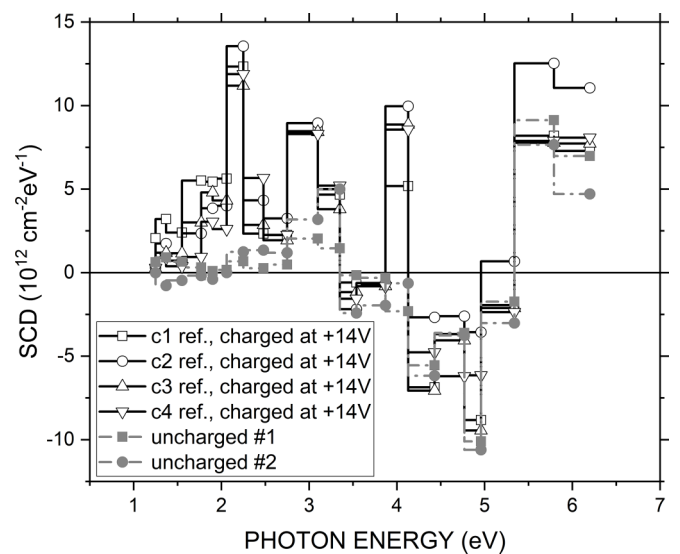


FIG. 5. Reference SCD spectra measured on several unheated *n*-Si/5-nm SiO₂/20-nm HfO₂/15-nm Au samples. Solid lines with open symbols and dashed lines with filled symbols represent charged and uncharged samples, respectively.

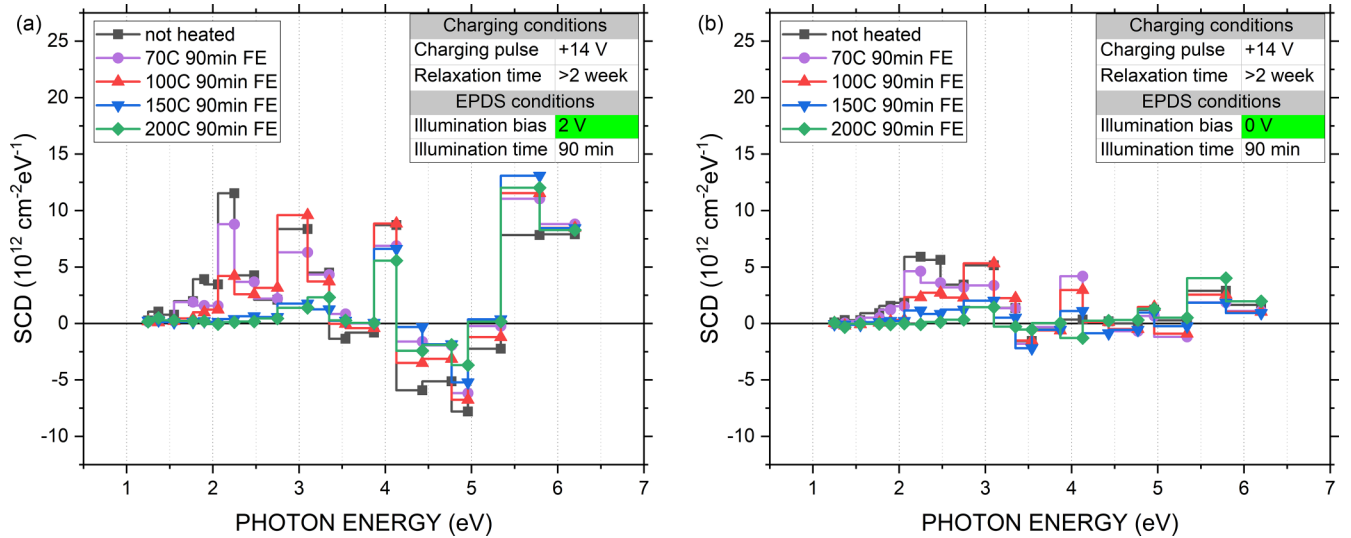


FIG. 6. SCD versus photon energy plots at different bias applied during sample illumination: +2 V (a) and 0 V (b), from the samples heated to 70 °C (purple), 100 °C (red), 150 °C (blue), or 200 °C (green) as compared to the reference unheated samples (black). The charging and photodepopulation conditions are indicated in the table on both panels.

BCB) are reproduced and may serve as markers to compare with the thermally treated samples.

We should note that the EPDS sensitivity range in this work is limited to photon energies below 4 eV, as the photodepopulation process may interfere with internal photoemission (IPE) of electrons from the Si substrate (corresponds to negative SCD values above 4 eV) and photogeneration of electron-hole pairs in HfO_2 (corresponds to intense depopulation peaks above 5.6 eV) [23,25,26,29]. The sharp peak around 4 eV likely indicates the deep trap level with a strong detrapping signal that overcomes the trapping of electrons photoinjected from the Si substrate, as discussed in [28]. These interfering processes generally do not allow for reliable quantification of deep traps ($E_{\text{opt}} > 4 \text{ eV}$).

When EPDS is performed on the thermally treated sample, the SCD values in each studied photon energy interval can be compared to the reference spectra. With increasing temperature, more deep trap levels will be emptied during heating, resulting in decrease/disappearance of the detrapping peaks in the EPDS spectrum, as shown in Fig. 6. It can be noticed that, for the samples treated at 70 °C or 100 °C for 90 min, the SCD spectrum is similar to the reference one, and only traps between 1.25 eV and 2.5 eV are (partially) affected by the thermal emission. By contrast, for the samples heated to 150 °C or 200 °C, most of the traps up to 4 eV energy depth are depopulated. This trend is reproduced for both studied gate bias conditions: +2 V and 0 V, Fig. 6, cf. panels (a) and (b), respectively. The only significant difference between these spectra is in the detrapped charge density. This result indicates a more efficient collection of the emitted electrons at the top electrode under external bias conditions and hints at the non-negligible retrapping process, which competes with the escape of the emitted electrons to the gate electrode through tail states near the HfO_2 BCB.

To determine the optical excitation energy corresponding to the thermal excitation energy at the given heating temperature, it is necessary to find the first optical energy

level unaffected by thermal emission. Taking into account the sensitivity range of EPDS experiments and possible retrapping of thermally depopulated electrons due to the “floating” electrode condition, one can estimate the following relationships from the trap depopulation viewpoint: heating at 70 °C roughly corresponds to illumination with the photon energy $\approx 2.3 \text{ eV}$, and heating at 100 °C corresponds to the photon energy $\approx 2.6 \text{ eV}$. Heating at higher temperatures of 150 °C and 200 °C significantly affects all detrapping peaks up to 3.3 eV and hence exceeds the EPDS sensitivity window, preventing the determination of R .

The thermal activation energy for each temperature can be estimated using the same expression $E_{th} \approx kT \ln(\nu\tau)$, where τ is now equal to 90 minutes. For 70 °C this results in $E_{th} \approx 1.15 \text{ eV}$, and for 100 °C we estimate $E_{th} \approx 1.25 \text{ eV}$. Therefore, from the direct experimental comparison, we conclude that the optical excitation energy in HfO_2 is approximately 2 times higher than the thermal excitation energy for the same type of electron trap. Taking into account fitting errors and the resolution of EPDS technique, we estimate R to be in the range 1.75–2.25; hence, it is still in a good agreement with previous theoretical predictions [26,29,31]. On the other hand, for higher heating temperature data point, 150 °C, the estimated thermal energy $E_{th} \approx 1.42 \text{ eV}$, suggesting that for exceeding optical value of 3.3 eV the ratio R should be close to 2.3 or above. This can be explained by a smaller contribution of retrapping of thermally depopulated electrons at higher temperatures, which would be more prone to escape to the metal gate. Similar consideration is also applicable to the 200 °C dataset.

For further verification of the extracted empirical ratio between the two energies, the heating-EPDS experiments were repeated for 70 °C and 100 °C heating for 1.5 hours without the “floating” electrode condition, i.e., with the sample connected to the measurement circuit during heating time with the 0 V or +3 V bias applied to the gate electrode. One can expect that at the 0 V bias conditions trap energy levels will be less

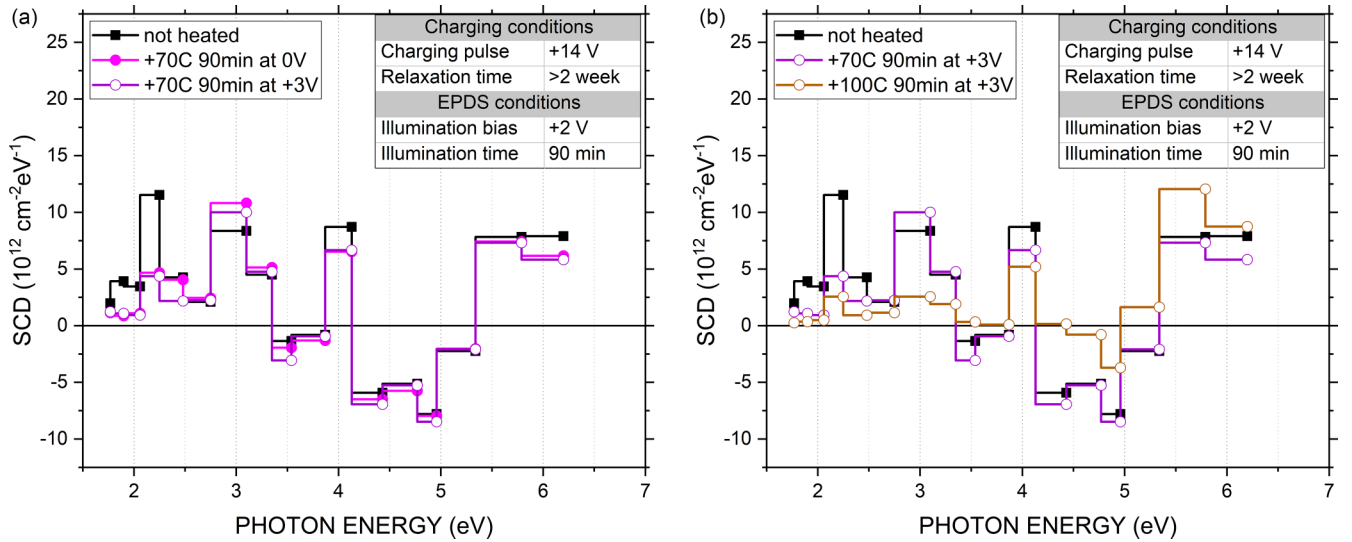


FIG. 7. Averaged SCD versus photon energy plots (in color) from the samples heated for 1.5 hours without “floating” electrode condition with (a) variable bias during heating at 70 °C and (b) heated at variable temperature, 70 °C or 100 °C, while keeping +3 V applied to the top electrode. The reference EPDS spectrum is shown in black on each panel. The experimental conditions are listed in the table on each panel.

depopulated compared to Fig. 6, panel (a), and at +3 V bias there can be positive shift in the post-heating EPDS spectrum (to account for field-induced emission during heating). The results for 70 °C and 100 °C 1.5 hours’ heating under different gate bias conditions are compared in Fig. 7. As one can see from Fig. 7(a), biasing the sample during heating does not cause significant changes in the EPDS spectrum, indicating only a marginal effect of the electric-field-induced emission component. Figure 7(b) shows that, when the samples are connected to the measurement circuit during heating at both studied temperatures (70 °C and 100 °C), the thermal emission efficiency is sufficiently high to depopulate traps with the optical energy levels at 2.25 eV and 3.1 eV. This is in sharp contrast to the “floating” electrode case, where these peaks were virtually unchanged for the corresponding heating conditions. This result suggests that the inferred optical energy threshold is actually approximately 0.25–0.5 eV higher, thus effectively increasing the empirical value of R to 2.2 ± 0.3 .

IV. THEORETICAL ANALYSIS

EPDS spectra are consistent with the results of previous studies [25,29], which have suggested that the negative charge in the bulk of a -HfO₂ is not impurity related, and can be associated with intrinsic electron traps and O vacancies. These electrons are trapped at precursor sites formed by undercoordinated Hf cations and elongated Hf-O bonds which are present in a -HfO₂ due to disorder and occur in a concentration of approximately 1 per 100 atoms. The electronic character and depth of these intrinsic traps, as well as oxygen vacancies, are determined by the significant polarization of the amorphous oxide network [29,31,60]. The intrinsic trapping sites can be found easily as negatively charging the periodic cell (increasing the number of electrons by one) leads to the electron being spontaneously localized into these deep states and the amorphous structure being polarized by the localized charge. Although electrons trapped at

vacancies or into intrinsic trapping sites are not, strictly speaking, self-trapped polarons, they exhibit polaronic character, i.e., coupling between the electron localization and distortion of the surrounding amorphous network. As discussed in [32,33], the small polaron optical absorption energy in crystals should be approximately twice the polaron trapping energy. Further considerations in [61] for small hole polarons suggest that optical energy should be increased by the value of polaron transfer integral between adjacent sites (typically about 0.1 eV). These predictions agree quite well with experimental values for hole polarons localized on O ions [62]. The DFT-calculated R values for hole polarons in crystals are very close to 2.0 [34–37]. Their validity for electron polarons in crystals has not been addressed experimentally so far, and it remains unclear how much they can be stretched in the case of polaronic states in amorphous materials. The recent results and discussion of electron localization in liquid water, which also give the R value close to 2.0, are very interesting in this regard [63].

Structural disorder of a -HfO₂ means that the electron trapping sites are not equivalent. Therefore, we expect the distributions of both thermal and optical ionization energies to be caused by disorder. In particular, the electron trapping energies calculated in a -HfO₂ [53] range within 0.5 eV. Below, we consider how the results of theoretical calculations of R for electrons trapped at precursor sites in a -HfO₂ agree with the experimental and theoretical results outlined above.

A. Effective mode approximation

Electron transitions between trap states and the oxide CB cause displacements of the atoms in the lattice from their original equilibrium positions due to the change in charge state of the defect. This can be described in terms of the activation of normal modes. Within the harmonic approximation, the energy cost of straining the lattice is decomposed into these lattice modes and has quadratic dependence on the amplitude

of displacement,

$$E = \sum_i \frac{1}{2} m_i \omega_i^2 \Delta Q_i^2, \quad (1)$$

where i is the index of the mode, m_i is the modal mass, ω_i is the normal mode's frequency of oscillation, and ΔQ_i is the amplitude of displacement of mode i from the equilibrium point. In practice, it is difficult to analyze thermal transitions in this way owing to the huge number of normal modes involved. Therefore, the sum over all modes is often replaced with a single *effective* mode, that is,

$$\sum_i \frac{1}{2} m_i \omega_i^2 \Delta Q_i^2 = \frac{1}{2} m_{\text{eff}} \omega_{\text{eff}}^2 \Delta Q_{\text{eff}}^2. \quad (2)$$

The crucial question then becomes the selection of the effective mode. In this approximation, the mode is equivocated with the displacements associated with the relaxation of the defect upon carrier trapping/detrapping. For example, upon emission of an electron from a trap into the CB, there is a set of atomic displacements, $\{\Delta \mathbf{R}_j^{(0)}\}$, between the two equilibrium points. In the effective mode approximation, this set of displacements is treated as a single mode, such that $\Delta Q_{\text{eff}}^{(0)} = (\Delta \mathbf{R}_1, \Delta \mathbf{R}_2, \dots) / \sum_i (\Delta \mathbf{R}_j^{(0)})^2$, where $\Delta \mathbf{R}_j$ is a displacement of atom j and is parallel to $\Delta \mathbf{R}_j^{(0)}$. The relaxation energy can then be understood as

$$E_{\text{rel}} = \frac{1}{2} m_{\text{eff}} \omega_{\text{eff}}^2 (\Delta Q_{\text{eff}}^{(0)})^2. \quad (3)$$

The effective mode is normalized such that, when the set of atomic displacements is equal to the set of atomic displacements associated with the defect relaxation, $\Delta \mathbf{R}^{(0)}$, $\Delta Q_{\text{eff}}^{(0)} = \Delta Q_{\text{eff}}^{(0)} = 1$. The effective mass of the mode is calculated as $m_{\text{eff}} = \sum_j (m_{\text{atom}})_j (\Delta \mathbf{R}_j^{(0)})^2 / \sum_j (\Delta \mathbf{R}_j^{(0)})^2$, where $(m_{\text{atom}})_j$ is the mass of the atom j .

Using this approach, one can calculate the frequency of the effective mode associated with a given thermal transition and the corresponding energy quanta as $\hbar \omega_{\text{eff}}$. Transitions are then treated as the absorption and emission of a number of energy quanta of the effective harmonic mode. The Huang-Rhys factor, S , an indicator of the electron-phonon coupling strength, is given by $S = E_{\text{rel}} / \hbar \omega_{\text{eff}}$.

B. Results of calculations

To investigate the thermal emission processes of intrinsic traps in $a\text{-HfO}_2$, we use the approximations discussed above to analyze the trap states previously reported in [29,53] and shown in Fig. 8(a). In the emission process, an electron excited from the oxide trap under bias must be promoted into a mobile state to be collected on an electrode. In amorphous insulators, however, states at the CB edge are localized [31] and become fully delocalized only above the ME. In reality, however, there is some uncertainty in the mobility of electrons below ME in $a\text{-HfO}_2$ as it is in fact a gradual change rather than a literal "edge," as illustrated in Figs. 1(a) and 1(b). Electrons that are energetically below the ME may either become quickly trapped again and immobilized or be involved in transport via hopping between adjacent precursor states facilitated by applied bias (see the discussion in Ref. [64]).

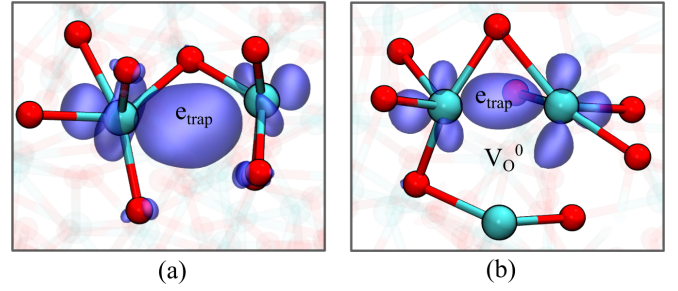


FIG. 8. An example of the local atomic configuration of electron traps in $a\text{-HfO}_2$. (a) shows a self-trapped electron in the bulk of $a\text{-HfO}_2$. (b) is the V_{O}^- defect, which is an extra electron trapped in a neutral oxygen vacancy. Cyan spheres indicate Hf ions; red spheres indicate O ions. The blue surface is an isosurface of the spin density of the trapped electron.

Below we compare thermal and optical excitation energies of an electron from a trap state into both the BCB state and a state at the ME. To determine the ME position, we performed inverse participation ratio (IPR) analysis of electronic states [29] and identified the lowest state where the CB wave function is completely delocalized. In our calculations, this state is by 0.5 eV higher than BCB.

The effective mode is identified by taking the fully relaxed geometry of the trap state (charge = -1) and the fully relaxed bulk neutral state as the geometry for the detrapped state. We note that, because of spontaneous electron trapping, the optimized geometry with the electron present corresponds to the localized trap state. Therefore the neutral state geometry in fact corresponds to the one for the electron at BCB, which in our calculations is the lowest unoccupied state. We then sample the local potential energy landscape around each configuration along the effective mode, fit to a quadratic function, and extract effective vibration frequencies. An example of the local PEC plotted for both charge states of the defect is shown in Fig. 9. The upper curves are produced by sampling along the effective mode in the neutral charge state, fitting to a quadratic polynomial, and then adding the BCB [Fig. 9(a)] or ME [Fig. 9(b)] eigenvalue. One can see that in both cases the crossing of PECs occurs at the minimum of the upper curve, which is consistent with the spontaneous electron trapping observed in self-consistent DFT calculations.

From the local expansion of the PEC shown in Fig. 9, we can obtain the thermal and optical ionization energies. E_{th} can be calculated by taking the difference between the two minima of the parabolas. Optical transitions can be determined by taking the vertical difference (at $\Delta Q_{\text{eff}} = 1$). Expanding the local harmonic potential of the set of five trap configurations, we find the average E_{th} of 0.9 eV and the average E_{opt} of 2.1 eV for transitions into the CB edge. To find the corresponding transitions into ME, the upper PEC is rigidly shifted up by 0.5 eV. Using these results, for the excitation into the ME we find the average E_{th} of 1.4 eV, and E_{opt} of 2.6 eV [see Fig. 9(b)]. This gives $R = 2.3$ for excitation into the BCB and $R = 1.9$ for excitation into the mobility edge. The electron conductivity during thermal and optical measurements will be by a combination of thermally activated and extended state band transport and will depend on carrier concentration,

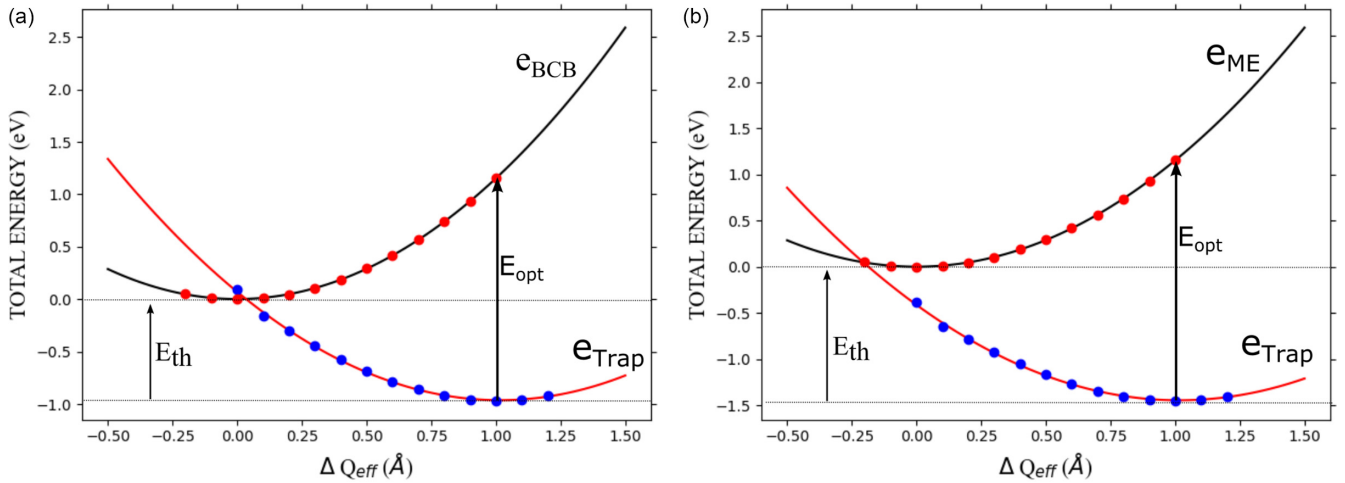


FIG. 9. Plots of the local PEC for electron capture into a trap state, in the single effective harmonic mode approximation. (a) Local PEC for capture of an electron from the BCB state. (b) Local PEC for capture of an electron from a CB state at the ME. The effective coordinate is defined so that $\Delta Q_{\text{eff}} = 0$ in the defect-free configuration and $\Delta Q_{\text{eff}} = 1$ for the ground state of the trapped electron.

as observed in [65]. Therefore, the average value of R will likely be between 1.9 and 2.3 and be distributed with some width.

For comparison, we also calculate E_{opt} using TDDFT. These calculations give slightly lower values for excitation to the BCB, with an average value of 1.9 eV. The decrease in E_{opt} likely happens due to the inclusion of the electron-hole interaction in TDDFT calculations, which is not present when calculating optical excitation energies by vertical energy changes in plots like those of Fig. 9. For excitations to the mobility edge, the TDDFT calculations give the same average value of 2.6 eV. Since the ME states are delocalized, the electron-hole interaction is smaller and we therefore do not expect as large a difference between the two methods of calculating E_{opt} . ω_{eff} is related to the curvature of the parabolas shown in Fig. 9. We find an average ω_{eff} of $2.4 \times 10^{13} \text{ s}^{-1}$ in the -1 charge state and $2.6 \times 10^{13} \text{ s}^{-1}$ for the neutral charge state. Using these frequencies to calculate the thermal activation energies does not change our conclusions.

Similar analysis was performed for negatively charged oxygen vacancy. In the neutral vacancy, 2 electrons are shared between Hf ions that neighbor the missing oxygen site. The -1 charged oxygen vacancies have an extra electron trapped onto these Hf ions, bringing the total number of electrons localized around the vacancy to three. The trapped electron state is very similar to the intrinsic trap [Fig. 8(b)], and has an average E_{th} of 0.8 eV and 1.3 eV for excitation into BCB and ME, respectively. The values for E_{opt} are 1.7 and 2.2 eV, respectively. The R values are thus similar for both the intrinsic trap and the V_{O}^- defect consistent with their polaronic nature [60].

Finally, we note that single- and bielectron traps can contribute to the EPDS and SCD spectra discussed above [29]. The calculations presented in [29] demonstrate that optical ionization energies of these traps overlap and that trapping of the second electron at the preexisting trap is spontaneous. Therefore, we do not expect significant differences between the behavior of single-electron traps described in Fig. 9 and bielectron traps.

V. DISCUSSION AND CONCLUSIONS

Our experimental results demonstrate that, using two different electron excitation mechanisms, we can access the same deep traps with energy levels inside the HfO₂ band gap; i.e., these electron traps are both optically and thermally active and are likely of the same nature. Next, we demonstrate that optical-to-thermal trap energy depth ratio R can be determined with reasonable accuracy and is equal to 2.2 ± 0.3 . Both the value and uncertainty of this result are consistent with the polaronic nature of the probed electron traps and supported by the results of theoretical calculations. If electron trapping/detrapping occurs in a process represented by Fig. 9(a), and both parabolas have the same frequency, $R = 2$ is expected. Excitations to deeper CB states (the mobility edge, for example) will result in R slightly less than 2. If the upper PEC is lower in energy, this presents a barrier for trapping and also causes R to significantly exceed 2. Therefore, R values around 2 indicate the formation of polaronic states and also characterize the excitation process. The average value of $R = 2.2$ can be interpreted as electrons in the states close to BCB in the applied bias can be swept to the electrode and can contribute to the observed charge removal.

Theoretical calculations include a degree of uncertainty, due to both the disorder and to the approximations used to fit the PECs. To test the validity of the harmonic approximation, we fitted the data to a third-order polynomial. However, we find that third-order coefficients are significantly smaller, of the order of $<5\%$ than the second-order coefficients, suggesting that a harmonic potential is a good approximation. The other major approximation made in this analysis is the use of a single effective mode, rather than the full normal-mode spectrum, which is made to make the analysis tractable. Some assessment of the accuracy of this approach has been carried out in the context of line-shape calculations for optical absorption [66]. It was suggested that the 1D approximation is accurate for defects with $S \gg 1$. In our case, an average $\hbar\omega$ is equal 0.03 eV and an average relaxation energy is 1.0 eV,

which gives $S \approx 33$, supporting that the 1D approximation is reasonable.

Our results provide the experimental methodology and theoretical justification to consistently link the thermal and optical energies of electron traps and describe their distribution in the band gap of amorphous oxide, such as HfO_2 . The latter is vital for our understanding of degradation mechanisms and mitigating reliability issues, such as gate leakage and P/NBTI. Industry often relies on compact models implemented in software, such as Ginestra [67–69] and Comphy [70], to assess the trap profile in the band gap of gate dielectrics. This is achieved by modeling the defect’s impact on MOS transistor electrical characteristics under different temperature and stress conditions and fitting the relevant experimental data. Because in such experiments the defect impact would be limited to the “visible” traps closely aligned with the semiconductor Fermi level, this effectively reduces the sensing range of the compact model approach to a small portion of the oxide band gap. Our results demonstrate that the distribution of trap levels in the band gap of amorphous HfO_2 is wide and originates from a family of defect bands. At certain electrostatic conditions, this can significantly affect the performance of various microelectronic devices, causing

V_{th} instability of HKMG FETs, facilitating gate leakage in scaled logic devices utilizing high- κ gate oxides, and reducing retention of charge-trapping FLASH memory devices with high- κ layers used in the gate stack for field enhancement and prolonged charge storage [71]. Furthermore, accurately mapping the distribution of trap energies in a wider energy range is critically important for building models of MOS devices employing wide gap semiconductors, such as In_2O_3 [72], indium-gallium-zinc oxide (IGZO) [73,74], SiC, and GaN, in combination with high- κ insulating oxides. In contrast to the compact modeling approach, the data presented in this work were obtained by directly probing the electron traps across the entire HfO_2 band gap. These data can be used as reference in various device characterization and modeling applications to help expand and improve the reliability modeling framework.

ACKNOWLEDGMENTS

Via the membership of J.S. and A.S. in the UK’s HEC Materials Chemistry Consortium, which is funded by EPSRC (Grant No. EP/X035859), this work used the ARCHER2 UK National Supercomputing Service [75]. J.S. and A.S. acknowledge support from EPSRC Grant No. EP/R034540/1.

-
- [1] C. Auth *et al.*, 45nm high-k + metal gate strain-enhanced transistors, in *2008 Symposium on VLSI Technology* (IEEE, 2008), pp. 128–129.
 - [2] M. M. Frank, High-k/metal gate innovations enabling continued CMOS scaling, in *2011 Proceedings of the European Solid-State Device Research Conference (ESSDERC)* (IEEE, 2011), pp. 25–33.
 - [3] R. M. Luna-Sánchez and I. González-Martínez, HfAlO and HfSiO based dielectrics for future DRAM applications, *ECS Trans.* **2**, 217 (2006).
 - [4] R. D. Clark, Emerging applications for high k materials in VLSI technology, *Materials* **7**, 2913 (2014).
 - [5] T. S. Böske, J. Müller, D. Bräuhaus, U. Schröder, and U. Böttger, Ferroelectricity in hafnium oxide thin films, *Appl. Phys. Lett.* **99**, 102903 (2011).
 - [6] 2009 International Technology Roadmap for Semiconductors (ITRS), <https://www.semiconductors.org/resources/2009-international-technology-roadmap-for-semiconductors-itsr>.
 - [7] M. T. Bohr, R. S. Chau, T. Ghani, and K. Mistry, The high-k solution, *IEEE Spectrum* **44**, 29 (2007).
 - [8] G. Ribes, J. Mitard, M. Denais, S. Bruyere, F. Monsieur, C. Parthasarathy, E. Vincent, and G. Ghibaudo, Review on high-k dielectrics reliability issues, *IEEE Trans. Device Mater. Reliabil.* **5**, 5 (2005).
 - [9] G. Ribes, M. Rafik, and D. Roy, Reliability issues for nano-scale CMOS dielectrics, *Microelectron. Eng.* **84**, 1910 (2007).
 - [10] A. Kerber and E. A. Cartier, Reliability challenges for CMOS technology qualifications with hafnium oxide/titanium nitride gate stacks, *IEEE Trans. Device Mater. Reliabil.* **9**, 147 (2009).
 - [11] S. Zafar, A. Kumar, E. Gusev, and E. Cartier, Threshold voltage instabilities in high- κ gate dielectric stacks, *IEEE Trans. Device Mater. Reliabil.* **5**, 45 (2005).
 - [12] E. Cartier *et al.*, Fundamental aspects of HfO_2 -based high-k metal gate stack reliability and implications on t_{inv} -scaling, in *2011 International Electron Devices Meeting* (IEEE, 2011), pp. 18.4.1–18.4.4.
 - [13] M. Pesic, F. P. G. Fengler, S. Slesazek, U. Schroeder, T. Mikolajick, L. Larcher, and A. Padovani, Root cause of degradation in novel HfO_2 -based ferroelectric memories, in *2016 IEEE International Reliability Physics Symposium (IRPS)* (IEEE, 2016), pp. MY-3-1–MY-3-5.
 - [14] M. N. K. Alam, B. Kaczer, L. Ragnarsson, M. Popovici, G. Rzepa, N. Horiguchi, M. Heyns, and J. Van Houdt, On the characterization and separation of trapping and ferroelectric behavior in HfZrO FET, *IEEE J. Electron Devices Soc.* **7**, 855 (2019).
 - [15] H. Mulaosmanovic *et al.*, Interplay between switching and retention in HfO_2 -based ferroelectric FETs, *IEEE Trans. Electron Devices* **67**, 3466 (2020).
 - [16] N. Zagni, F. M. Puglisi, P. Pavan, and M. A. Alam, Reliability of HfO_2 -based ferroelectric FETs: A critical review of current and future challenges, *Proc. IEEE* **111**, 158 (2023).
 - [17] D. P. Ioannou, HKMG CMOS technology qualification: The PBTI reliability challenge, *Microelectron. Reliab.* **54**, 1489 (2014).
 - [18] M. B. Zahid, D. R. Aguado, R. Degraeve, W. C. Wang, B. Govoreanu, M. Toledano-Luque, V. V. Afanas’ev, and J. Van Houdt, Applying complementary trap characterization technique to crystalline γ -phase- Al_2O_3 for improved understanding of nonvolatile memory operation and reliability, *IEEE Trans. Electron Devices* **57**, 2907 (2010).
 - [19] K. L. Brower, Structural features at the Si- SiO_2 interface, *Z. Phys. Chem.* **151**, 177 (1987).
 - [20] A. Stesmans and V. Afanas’ev, Defect correlated with positive charge trapping in functional HfO_2 layers on (100)Si revealed

- by electron spin resonance: Evidence for oxygen vacancy? *Microelectron. Eng.* **178**, 112 (2017).
- [21] C. Gionco, S. Livraghi, S. Maurelli, E. Giamello, S. Tosoni, C. Di Valentin, and G. Pacchioni, Al- and Ga-doped TiO₂, ZrO₂, and HfO₂: The nature of O 2p trapped holes from a combined electron paramagnetic resonance (EPR) and density functional theory (DFT) study, *Chem. Mater.* **27**, 3936 (2015).
- [22] S. J. Moxim, J. P. Ashton, M. A. Anders, and J. T. Ryan, Combining electrically detected magnetic resonance techniques to study atomic-scale defects generated by hot-carrier stressing in HfO₂/SiO₂/Si transistors, *J. Appl. Phys.* **133**, 145702 (2023).
- [23] V. V. Afanas'ev, W. C. Wang, F. Cerbu, O. Madia, M. Houssa, and A. Stesmans, Spectroscopy of deep gap states in high-k insulators, *ECS Trans.* **64**, 17 (2014).
- [24] W. C. Wang, M. Badylevich, V. V. Afanas'ev, A. Stesmans, C. Adelman, S. Van Elshocht, J. A. Kittl, M. Lukosius, C. Walczyk, and C. Wenger, Band alignment and electron traps in Y₂O₃ layers on (100)Si, *Appl. Phys. Lett.* **95**, 132903 (2009).
- [25] F. Cerbu, O. Madia, D. Andreev, S. Fadida, M. Eizenberg, L. Breuil, J. Lisoni, J. Kittl, J. Strand, A. Shluger *et al.*, Intrinsic electron traps in atomic-layer deposited HfO₂ insulators, *Appl. Phys. Lett.* **108**, 222901 (2016).
- [26] R. A. Izmailov, J. W. Strand, L. Larcher, B. J. O'Sullivan, A. L. Shluger, and V. V. Afanas'ev, Electron trapping in ferroelectric HfO₂, *Phys. Rev. Mater.* **5**, 034415 (2021).
- [27] R. Izmailov, B. O'Sullivan, M. Popovici, J. Kittl, and V. Afanas'ev, Shallow electron traps in high-k insulating oxides, *Solid-State Electron.* **183**, 108052 (2021).
- [28] R. Izmailov, B. O'Sullivan, M. Popovici, and V. Afanas'ev, Deep electron traps in HfO₂-based ferroelectrics: (Al/Si-doped) HfO₂ versus HfZrO₄, *Solid-State Electron.* **194**, 108388 (2022).
- [29] J. Strand, M. Kaviani, V. V. Afanas'ev, J. G. Lisoni, and A. L. Shluger, Intrinsic electron trapping in amorphous oxide, *Nanotechnology* **29**, 125703 (2018).
- [30] B. J. O'Sullivan, V. Putcha, R. Izmailov, V. Afanas'ev, E. Simoen, T. Jung, Y. Higashi, R. Degraeve, B. Truijen, B. Kaczer *et al.*, Defect profiling in FEFET Si : HfO₂ layers, *Appl. Phys. Lett.* **117**, 203504 (2020).
- [31] J. Strand, M. Kaviani, D. Gao, A.-M. El-Sayed, V. V. Afanas'ev, and A. L. Shluger, Intrinsic charge trapping in amorphous oxide films: Status and challenges, *J. Phys.: Condens. Matter* **30**, 233001 (2018).
- [32] D. Emin, Optical properties of large and small polarons and bipolarons, *Phys. Rev. B* **48**, 13691 (1993).
- [33] J. J. Markham, Interaction of normal modes with electron traps, *Rev. Mod. Phys.* **31**, 956 (1959).
- [34] B. Himmetoglu, A. Janotti, L. Bjaalie, and C. G. Van de Walle, Interband and polaronic excitations in YTiO₃ from first principles, *Phys. Rev. B* **90**, 161102(R) (2014).
- [35] L. Bjaalie, D. G. Ouellette, P. Moetakef, T. A. Cain, A. Janotti, B. Himmetoglu, S. J. Allen, S. Stemmer, and C. G. Van de Walle, Small hole polarons in rare-earth titanates, *Appl. Phys. Lett.* **106**, 232103 (2015).
- [36] J. L. Lyons, Self-trapped holes and polaronic acceptors in ultrawide-bandgap oxides, *J. Appl. Phys.* **131**, 025701 (2022).
- [37] J. R. De Lile, A. Bahadoran, S. Zhou, and J. Zhang, Polaron in TiO₂ from first-principles: A review, *Adv. Theory Simul.* **5**, 2100244 (2022).
- [38] A. M. Stoneham, *Theory of Defects in Solids* (Clarendon Press, Oxford, 1975).
- [39] Z. Barandiarán, A. Meijerink, and L. Seijo, Configuration coordinate energy level diagrams of intervalence and metal-to-metal charge transfer states of dopant pairs in solids, *Phys. Chem. Chem. Phys.* **17**, 19874 (2015).
- [40] C. Di Valentin and G. Pacchioni, Spectroscopic properties of doped and defective semiconducting oxides from hybrid density functional calculations, *Acc. Chem. Res.* **47**, 3233 (2014).
- [41] M. Gerosa, C. E. Bottani, L. Caramella, G. Onida, C. Di Valentin, and G. Pacchioni, Defect calculations in semiconductors through a dielectric-dependent hybrid DFT functional: The case of oxygen vacancies in metal oxides, *J. Chem. Phys.* **143**, 134702 (2015).
- [42] J. Strand, S. K. Chulkov, M. B. Watkins, and A. L. Shluger, First principles calculations of optical properties for oxygen vacancies in binary metal oxides, *J. Chem. Phys.* **150**, 044702 (2019).
- [43] S. Pandey, A. Shukla, and A. Tripathi, Elucidating the influence of native defects on electrical and optical properties in semiconducting oxides: An experimental and theoretical investigation, *Comput. Mater. Sci.* **210**, 111037 (2022).
- [44] S. Bhandari, J. L. Lyons, D. Wickramaratne, and M. E. Zvanut, Optical transitions of neutral Mg in Mg-doped β -Ga₂O₃, *APL Mater.* **10**, 021103 (2022).
- [45] N. Mott, The mobility edge since 1967, *J. Phys. C: Solid State Phys.* **20**, 3075 (1987).
- [46] E. H. Nicollian and J. R. Brews, *MOS (Metal Oxide Semiconductor) Physics and Technology* (Wiley, New York, 1982).
- [47] W.-C. Lee and C. Hu, Modeling gate and substrate currents due to conduction- and valence-band electron and hole tunneling [CMOS technology], in *2000 Symposium on VLSI Technology. Digest of Technical Papers (Cat. No. 00CH37104)* (IEEE, 2000), pp. 198–199.
- [48] A. S. Konashuk, E. O. Filatova, A. V. Bugaev, S. S. Sakhonenkov, and D. V. Danilov, Role of postdeposition annealing and doping with Si and Al impurities in the formation of Hf_xSi_{1-x}O₂ at the SiO₂/FE : HfO₂ interface in a ferroelectric field-effect transistor, *J. Phys. Chem. C* **127**, 9759 (2023).
- [49] J. VandeVondele, M. Krack, F. Mohamed, M. Parrinello, T. Chassaing, and J. Hutter, Quickstep: Fast and accurate density functional calculations using a mixed Gaussian and plane waves approach, *Comput. Phys. Commun.* **167**, 103 (2005).
- [50] S. Goedecker, M. Teter, and J. Hutter, Separable dual-space Gaussian pseudopotentials, *Phys. Rev. B* **54**, 1703 (1996).
- [51] J. VandeVondele and J. Hutter, Gaussian basis sets for accurate calculations on molecular systems in gas and condensed phases, *J. Chem. Phys.* **127**, 114105 (2007).
- [52] M. Guidon, J. Hutter, and J. VandeVondele, Robust periodic Hartree-Fock exchange for large-scale simulations using Gaussian basis sets, *J. Chem. Theory Comput.* **5**, 3010 (2009).
- [53] M. Kaviani, J. Strand, V. V. Afanas'ev, and A. L. Shluger, Deep electron and hole polarons and bipolarons in amorphous oxide, *Phys. Rev. B* **94**, 020103(R) (2016).
- [54] M. Guidon, J. Hutter, and J. VandeVondele, Auxiliary density matrix methods for Hartree-Fock exchange calculations, *J. Chem. Theory Comput.* **6**, 2348 (2010).
- [55] O. A. Dicks, J. Cottom, A. L. Shluger, and V. V. Afanas'ev, The origin of negative charging in amorphous Al₂O₃ films: The role of native defects, *Nanotechnology* **30**, 052021 (2019).
- [56] G. Broglia, G. Ori, L. Larcher, and M. Montorsi, Molecular dynamics simulation of amorphous HfO₂ for resistive RAM

- applications, *Modelling Simul. Mater. Sci. Eng.* **22**, 065006 (2014).
- [57] T. R. Durrant, S. T. Murphy, M. B. Watkins, and A. L. Shluger, Relation between image charge and potential alignment corrections for charged defects in periodic boundary conditions, *J. Chem. Phys.* **149**, 024103 (2018).
- [58] S. Lany and A. Zunger, Assessment of correction methods for the band-gap problem and for finite-size effects in supercell defect calculations: Case studies for ZnO and GaAs, *Phys. Rev. B* **78**, 235104 (2008).
- [59] H. M. Przewlocki, T. Gutt, and K. Piskorski, The inflection point of the capacitance-voltage, $C(V_G)$, characteristic and the flat-band voltage of metal-oxide-semiconductor structures, *J. Appl. Phys.* **115**, 204510 (2014).
- [60] J. Gavartin, D. Muñoz Ramo, A. Shluger, G. Bersuker, and B. Lee, Negative oxygen vacancies in HfO_2 as charge traps in high- k stacks, *Appl. Phys. Lett.* **89**, 082908 (2006).
- [61] O. F. Schirmer, O^- bound small polarons in oxide materials, *J. Phys.: Condens. Matter* **18**, R667 (2006).
- [62] O. F. Schirmer, Holes bound as small polarons to acceptor defects in oxide materials: Why are their thermal ionization energies so high? *J. Phys.: Condens. Matter* **23**, 334218 (2011).
- [63] P. Low, W. Chu, Z. Nie *et al.*, Observation of a transient intermediate in the ultrafast relaxation dynamics of the excess electron in strong-field-ionized liquid water, *Nat. Commun.* **13**, 7300 (2022).
- [64] N. F. Mott, The conductivity near a mobility edge, *Philos. Mag. B* **49**, L75 (1984).
- [65] C.-G. Lee, B. Cobb, and A. Dodabalapur, Band transport and mobility edge in amorphous solution-processed zinc tin oxide thin-film transistors, *Appl. Phys. Lett.* **97**, 203505 (2010).
- [66] A. Alkauskas, J. L. Lyons, D. Steiauf, and C. G. Van de Walle, First-principles calculations of luminescence spectrum line shapes for defects in semiconductors: The example of GaN and ZnO, *Phys. Rev. Lett.* **109**, 267401 (2012).
- [67] A. Padovani, B. Kaczer, M. Pešić, A. Belmonte, M. Popovici, L. Nyns, D. Linten, V. V. Afanas'ev, I. Shlyakhov, Y. Lee, H. Park, and L. Larcher, A sensitivity map-based approach to profile defects in MIM capacitors from I - V , C - V , and G - V measurements, *IEEE Trans. Electron Devices* **66**, 1892 (2019).
- [68] MDLsoft, *Manual: Physics of Carrier Transport in Ginestra* (MDLsoft, Santa Clara, CA, 2018).
- [69] MDLsoft, Inc., Santa Clara, CA.
- [70] G. Rzepa *et al.*, Comphy – A compact-physics framework for unified modeling of BTI, *Microelectron. Reliabil.* **85**, 49 (2018).
- [71] L. Breuil, M. Popovici, J. Stiers, A. Arreghini, S. Ramesh, G. V. D. Bosch, J. V. Houdt, and M. Rosmeulen, Optimization of retention in ferroelectricity boosted gate stacks for 3D NAND, in *2023 IEEE International Memory Workshop (IMW)* (IEEE, 2023), pp. 1–4.
- [72] M. Si, Z. Lin, Z. Chen, X. Sun, H. Wang, and P. D. Ye, Scaled indium oxide transistors fabricated using atomic layer deposition, *Nat. Electron.* **5**, 164 (2022).
- [73] A. Chasin *et al.*, Understanding and modelling the PBTI reliability of thin-film IGZO transistors, in *2021 IEEE International Electron Devices Meeting (IEDM)* (IEEE, 2021), pp. 31.1.1–31.1.4.
- [74] Z. Wu *et al.*, Characterizing and modelling of the BTI reliability in IGZO-TFT using light-assisted I - V spectroscopy, in *2022 International Electron Devices Meeting (IEDM)* (IEEE, 2022), pp. 30.1.1–30.1.4.
- [75] See <http://www.archer2.ac.uk>.